

# Thermoelectric Performance of the Half-Heusler Phases $RNiSb$ ( $R = Sc, Dy, Er, Tm, Lu$ ): High Mobility Ratio between Majority and Minority Charge Carriers

K. Ciesielski<sup>1,\*</sup>, K. Synoradzki<sup>1</sup>, I. Veremchuk<sup>2,†</sup>, P. Skokowski<sup>3</sup>, D. Szymański<sup>1</sup>,  
Yu. Grin<sup>2</sup>, and D. Kaczorowski<sup>1</sup>

<sup>1</sup>*Institute of Low Temperature and Structure Research, Polish Academy of Sciences, P.O. Box 1410,  
50-950 Wrocław, Poland*

<sup>2</sup>*Max-Planck-Institut für Chemische Physik fester Stoffe, 01187 Dresden, Germany*

<sup>3</sup>*Institute of Molecular Physics, Polish Academy of Sciences, Smoluchowskiego 17, 60-179 Poznań, Poland*



(Received 8 August 2020; revised 16 September 2020; accepted 7 October 2020; published 19 November 2020)

Deeper understanding of electrical and thermal transport is critical for further development of thermoelectric materials. Here we describe the thermoelectric performance of a group of rare-earth-bearing half-Heusler phases determined in a wide temperature range. Polycrystalline samples of  $ScNiSb$ ,  $DyNiSb$ ,  $ErNiSb$ ,  $TmNiSb$ , and  $LuNiSb$  are synthesized by arc melting and densified by spark plasma sintering. They are characterized by powder x-ray diffraction and scanning electron microscopy. The physical properties are studied by means of heat-capacity and Hall-effect measurements performed in the temperature range from 2 to 300 K, as well as electrical-resistivity, Seebeck-coefficient, and thermal-conductivity measurements performed in the temperature range from 2 to 950 K. All the materials except  $TmNiSb$  are found to be narrow-gap intrinsic *p*-type semiconductors with rather light charge carriers. In  $TmNiSb$ , the presence of heavy holes with large weighted mobility is evidenced by the highest power factor among the series ( $17 \mu\text{W K}^{-2} \text{cm}^{-1}$  at 700 K). The experimental electronic relaxation time calculated with the parabolic band formalism is found to range from  $0.8 \times 10^{-14}$  to  $2.8 \times 10^{-14}$  s. In all the materials studied, the thermal conductivity is between 3 and 6  $\text{W m}^{-1} \text{K}^{-1}$  near room temperature (i.e., smaller than in other pristine *d*-electron half-Heusler phases reported in the literature). The experimental observation of the reduced thermal conductivity appears fully consistent with the estimated low sound velocity as well as strong point-defect scattering revealed by Debye-Callaway modeling. Furthermore, analysis of the bipolar contribution to the measured thermal conductivity yields abnormally large differences between the mobilities of *n*-type and *p*-type carriers. The latter feature makes the compounds examined excellent candidates for further optimization of their thermoelectric performance via electron doping.

DOI: [10.1103/PhysRevApplied.14.054046](https://doi.org/10.1103/PhysRevApplied.14.054046)

## I. INTRODUCTION

Half-Heusler (HH) phases are equiatomic compounds crystallizing in the cubic MgAgAs-type structure (space group  $F\bar{4}3m$ , no. 216) with composition  $MTZ$ , where  $M$  denotes an early transition metal, rare-earth element, or alkaline-earth metal,  $T$  stands for a late transition metal, and  $Z$  corresponds to a main-group element. For decades, this family of compounds has been extensively investigated from multiple perspectives. In recent years, HH phases have been studied particularly deeply in the context of possible nontrivial topology of their electronic

structure [1–3], coexistence of magnetism and superconductivity [4,5], heavy-fermion behaviour [6,7], and giant magnetoresistance [8,9], as well as their thermoelectric (TE) properties [10–13].

TE application appears to be of particularly high importance due to the contemporary global energy crisis. HH compounds are well suited for this purpose because of their high energy-conversion efficiency [10], accompanied by excellent mechanical properties [14] and outstanding thermal stability [15].

One of the widely recognized thermoelectric HH compounds is  $Hf_{1-x}Zr_xNiSn_{1-y}Sb_y$  [16]. The figure of merit [ $ZT = (S^2/\kappa\rho)T$ , where  $S$  denotes the Seebeck coefficient,  $\kappa$  corresponds to thermal conductivity, and  $\rho$  stands for electrical resistivity] exceeded in its case the critical border of unity [16]. Subsequently, the relation between the structural disorder and thermoelectric properties was extensively studied for ZrNiSn-based thermoelectrics

\*k.ciesielski@intibs.pl

<sup>†</sup>Current address: Institute of Ion Beam Physics and Material Research, Helmholtz-Zentrum Dresden-Rossendorf, 01328 Dresden, Germany.

[17–21]. To construct a device, however, *n*-type and *p*-type legs with similar properties are necessary. For almost a decade, intuition-driven research did not succeed in finding a high-*ZT* *p*-type counterpart from the HH group. Eventually, the border of *ZT* = 1 was crossed with *p*-type HH compounds as a result of in-depth studies. The most-prominent examples include ZrCoBi, in which enhanced TE performance was achieved due to high band degeneracy and low sound velocity [10], NbFeSb with heavy *p*-type charge carriers [22], and TaFeSb, which was discovered by an “inverse-design” *ab initio* search aimed at identifying materials with tailored functionalities [23].

These findings motivate us to continue in-depth research into alternative interesting subfamilies among HH phases. One such group is the rare-earth-bearing HH compounds  $RT^XZ^V$ , where  $R$  is a rare-earth element,  $T^X$  corresponds to a transition metal from the tenth group of the periodic table ( $T^X = \text{Ni, Pd, Pt}$ ), and  $Z^V = \text{Sb, Bi}$ . Literature data show that  $RT^XZ^V$  materials might possess lower thermal conductivity than their well-known *d*-electron counterparts when pristine ternary compounds are considered [24,25]. What is more, several reports revealed that rare-earth-bearing HH phases might exhibit sizable crystallographic disorder [26–29], which was previously determined as a beneficial feature for TE energy conversion of HH phases [30].

Stimulated by these hints, we perform a detailed study of thermoelectric transport for  $R\text{NiSb}$  compounds. As an extension to our research on high-temperature TE behavior of arc-melted  $R\text{NiSb}$  samples [31], here we report structural, electronic, and thermal properties of  $\text{DyNiSb}$ ,  $\text{ErNiSb}$ ,  $\text{TmNiSb}$ , and  $\text{LuNiSb}$  densified by spark plasma sintering (SPS) after arc melting. The most-important outcome is analysis of bipolar thermal conductivity with a simple, yet-underutilized model [32]. In conclusion, the model encourages electron doping for  $R\text{NiSb}$  compounds due to superior mobility predicted for the *n*-type carriers. The results of our investigations are discussed together with those obtained recently for SPS-treated  $\text{ScNiSb}$  [26]. The present work is part of our larger project aimed at understanding the structural and magnetotransport properties of HH compounds  $RT^X\text{Sb}$  and  $RT^X\text{Bi}$  [33–41].

## II. EXPERIMENT

Polycrystalline samples of  $\text{DyNiSb}$ ,  $\text{ErNiSb}$ ,  $\text{TmNiSb}$ , and  $\text{LuNiSb}$  are synthesized by arc-melting elemental rare-earth metals (lumps, 99.9 at. %), nickel (rod, 99.99 at. %), and antimony (lumps, 99.999 at. %) on a copper hearth in an ultrapure (5N) argon atmosphere. Because of intensive evaporation of antimony during melting, approximately 6% of its nominal mass is added beforehand. Subsequently, the arc-melted buttons are annealed in an evacuated quartz tube at 973 K for 2 weeks. The so-obtained ingots are hand-ground into a fine powder. To obtain dense bulk samples suitable for measurement of TE properties, the

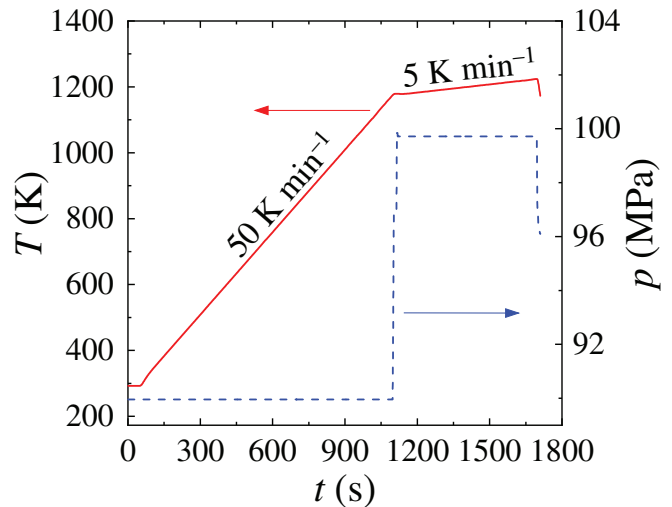


FIG. 1. Heating (red) and pressurizing (blue) cycles for  $R\text{NiSb}$  powders during spark plasma sintering.

spark-plasma-sintering technique is used (SPS-515 ET, Dr Sinter setup, SDC Fuji, Japan). The powders are loaded into graphite dies (diameter 10 mm) and heated to 1223 K at a rate of  $50 \text{ K min}^{-1}$  under uniaxial pressure of 90 MPa. Afterward, densification is continued by heating of the sample to 1273 K at a rate of  $5 \text{ K min}^{-1}$  under pressure of 100 MPa (see Fig. 1).

The samples after SPS treatment are characterized by powder XRD performed at room temperature with an X’pert Pro PANalytical diffractometer with  $\text{Cu K}\alpha$  radiation. The reflection positions obtained by profile deconvolution for  $R\text{NiSb}$  samples ( $R = \text{Dy, Er, Tm, Lu}$ ) are corrected with use of silicon as an internal standard ( $a = 0.54305 \text{ nm}$  at room temperature [42]). Crystal-structure refinements are done with the program WinCSD [43]. The compositions of the samples are determined by energy-dispersive x-ray spectroscopy (EDS) with an FEI scanning electron microscope equipped with an Apollo X silicon drift detector. For EDS analysis we use the spectral lines  $R L\alpha$  (where  $R = \text{Dy, Er, Tm, Lu}$ ),  $\text{Ni K}\alpha$ , and  $\text{Sb }L\alpha$  with a beam landing energy of 20 keV. The relative error of this technique is below 2%. The Archimedes method is applied to determine experimentally the density of the samples ( $d_{\text{expt}}$ ).

The Seebeck coefficient ( $S$ ) and the electrical resistivity ( $\rho$ ) are measured simultaneously under a helium atmosphere in the temperature range from 350 to 950 K by the temperature-differential method and the four-probe method, respectively, implemented in a Linseis LSR-3 apparatus. For each sample, several measurements are conducted with different constant-temperature gradients of 30, 40, and 50 K. All these measurements give the same results within an experimental accuracy of 3% for  $S$  and 5% for  $\rho$ . Therefore, in the following text, only the data obtained for the gradient of 50 K are presented.

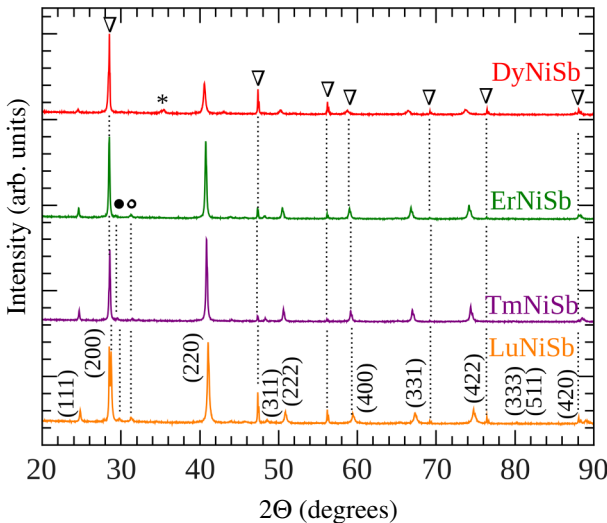


FIG. 2. XRD patterns for samples  $R\text{NiSb}$  ( $R = \text{Dy}, \text{Er}, \text{Tm}, \text{Lu}$ ). Triangles denote Bragg reflections from silicon standard, the asterisk corresponds to the impurity signal from the  $\text{Dy}_3\text{Ni}_6\text{Sb}_5$  phase, and open and closed circles stand for reflections from  $\text{NiSb}$  and the oxide  $\text{R}_2\text{O}_3$ , respectively.

The thermal diffusivity ( $D$ ) is measured in the temperature range from 300 to 923 K by the laser flash method (NETZSCH LFA 457). The thermal conductivity ( $\kappa$ ) is derived from the relationship  $\kappa = DC_p d_{\text{expt}}$ , where  $C_p = 3n_a R$  represents the specific heat ( $n_a$  is the number of atoms in a formula unit and  $R$  is the gas constant). The estimated uncertainty of  $\kappa$  is about 10%.

Low-temperature measurements of the electrical resistivity, specific heat, Seebeck coefficient, and thermal conductivity are performed in the temperature range from 2 to 300 K with a Quantum Design physical-property-measurement system (PPMS-9). The electrical resistivity is measured by the standard four-point dc technique. Electrical leads are made from Ag wires attached to the sample surface with use of silver-epoxy paste. The heat-capacity measurements are performed by the relaxation method and with the two- $\tau$  model. For the Seebeck-coefficient and thermal-conductivity studies, gold-plated copper electrodes are attached to the specimens with use of silver-epoxy paste. The experimental uncertainties in the low-temperature determination of  $\rho$ ,  $S$ , and  $\kappa$  are 0.01%, 5%, and 5%, respectively.

### III. RESULTS

#### A. Structural properties

All the major Bragg peaks in the XRD patterns of the prepared materials are easily indexed with the  $\text{MgAgAs}$ -type lattice (Fig. 2). The lattice parameters of the HH phases obtained are listed in Table I. They are in good agreement with the literature data [25,28,44]. For DyNiSb,

TABLE I. Structural parameters of  $R\text{NiSb}$  materials studied. Data for  $\text{ScNiSb}$  are acquired from Ref. [26].

$R\text{NiSb}$	$a$ (Å)	$V$ (Å <sup>3</sup> )	$d_{\text{theor}}$ (g cm <sup>-3</sup> )	$d_{\text{expt}}$ (g cm <sup>-3</sup> )
ScNiSb	6.0761(4)	224.32(5)	6.674(2)	6.58(1)
DyNiSb	6.2977(2)	249.49(9)	9.348(1)	8.78(2)
ErNiSb	6.2607(1)	245.61(5)	9.476(1)	9.22(5)
TmNiSb	6.2446(1)	243.67(4)	9.595(1)	9.30(7)
LuNiSb	6.2220(1)	240.93(1)	9.875(1)	9.73(3)

we observe Bragg reflections from impurities; the strongest one near  $2\Theta = 35^\circ$  is marked by an asterisk in Fig. 2. Careful analysis of the XRD pattern leads us to ascribe the extra peaks to a hitherto-unknown phase,  $\text{Dy}_3\text{Ni}_6\text{Sb}_5$ , that crystallizes with a monoclinic  $\text{Y}_3\text{Ni}_6\text{Sb}_5$ -type structure [45] [space group  $P12_1/m1$ , no. 11.  $a = 10.565(4)$  Å,  $b = 4.126(2)$  Å,  $c = 12.620(7)$  Å,  $\beta = 113.66(1)^\circ$ ]. Detailed study of the crystal structure and physical properties of  $\text{Dy}_3\text{Ni}_6\text{Sb}_5$  will be the subject of a separate study. For ErNiSb, TmNiSb, and LuNiSb, we observe traces of  $\text{NiSb}$  and  $\text{R}_2\text{O}_3$ , which are denoted by open and closed circles in Fig. 2, respectively. The SEM studies reveal that all the SPS-prepared  $R\text{NiSb}$  samples contain no gas cavities, pores, and/or microcracks. Exemplary results of the EDS imaging of polished surfaces for the TmNiSb sample are presented in Fig. 3 and tabulated in Table II. The chemical composition of the main phase (marked in Fig. 3 by points 1–3) is depleted in Ni and Sb. Areas 4–6 correspond to  $\text{NiSb}$  precipitation detected also by powder XRD, while points 7 and 8 correspond to either elemental Tm or small quantities of thulium oxide  $\text{Tm}_2\text{O}_3$ . All other  $R\text{NiSb}$  samples exhibit qualitatively similar tendencies in the chemical composition, except for DyNiSb, for which we observe

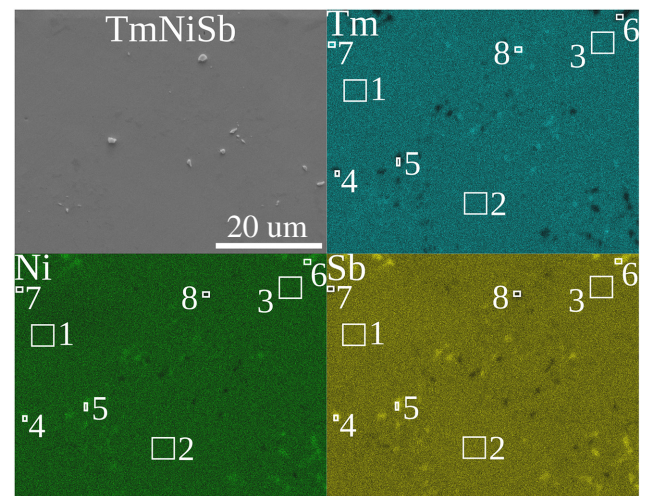


FIG. 3. SEM-EDS chemical mapping for TmNiSb. The scale bar applies for all panels. Quantitative analysis of the marked areas is given in Table II.

TABLE II. Results of the EDS imaging for TmNiSb. The listed areas correspond to those marked in Fig. 3.

Area	Tm (at. %)	Ni (at. %)	Sb (at. %)
1	36.56	30.15	33.29
2	37.33	30.24	32.43
3	37.75	27.56	34.69
		$\text{Tm}_{37(1)}\text{Ni}_{29(2)}\text{Sb}_{33(1)}$	
4	14.64	43.26	42.1
5	14.87	42.24	42.88
6	8.14	47.86	44
		$\text{Tm}_{13(4)}\text{Ni}_{44(3)}\text{Sb}_{43(1)}$	
7	63.78	15.15	21.06
8	70.13	15.64	14.23
		$\text{Tm}_{67(4)}\text{Ni}_{15(1)}\text{Sb}_{18(5)}$	

also a  $\text{Dy}_3\text{Ni}_6\text{Sb}_5$  phase in the EDS image. For each specimen, the pycnometric density is less than the theoretical density ( $d_{\text{theor}}$ ) calculated from the XRD data (see Table I). The relative mass density is always greater than 94%.

## B. Electrical properties

The results of electrical-transport measurements are summarized in Fig. 4(a). All the  $R\text{NiSb}$  samples are found to exhibit semiconducting behavior with the resistivity spanning a wide range from less than  $10 \mu\Omega \text{ m}$  near 950 K

for  $R\text{NiSb}$  ( $R = \text{Dy, Er, Tm, Lu}$ ) to  $2200 \mu\Omega \text{ m}$  at 2 K for  $\text{ScNiSb}$ . The decrease of  $\rho$  with rising temperature from 2 to 300 K observed for  $\text{ScNiSb}$ ,  $\text{TmNiSb}$ , and  $\text{LuNiSb}$  is associated with extrinsic activation of charge carriers [9]. In turn, metalliclike transport found for  $\text{ErNiSb}$  and  $\text{DyNiSb}$  in a similar temperature range likely arises from the large number of in-gap states created by crystallographic disorder. In this context, it is worth recalling that it was shown for semiconducting  $d$ -electron HH phases that their intrinsic energy gap vanishes for 15% antisite defects between  $4a$  and  $4b$  Wyckoff sites [46], and other defects were also calculated to reduce the band gap [47]. The topic was recently discussed from an experimental perspective for  $\text{TaGeIr}$  [48].

As can be inferred from Fig. 4(a), for each sample,  $\rho(T)$  forms a hump in the temperature region from 220 to 480 K, which likely signals saturation of extrinsic transport. Above 650 K, an exponential decrease of the resistivity with increasing temperature is seen, which is a characteristic feature of the intrinsic conductivity regime. These high-temperature data are approximated by the classical Arrhenius formula:

$$1/\rho = \sigma_0 \exp(-E_g/2k_B T), \quad (1)$$

where  $E_g$  stands for the intrinsic band gap and  $\sigma_0$  denotes the conductivity coefficient ( $k_B$  is the Boltzmann constant),

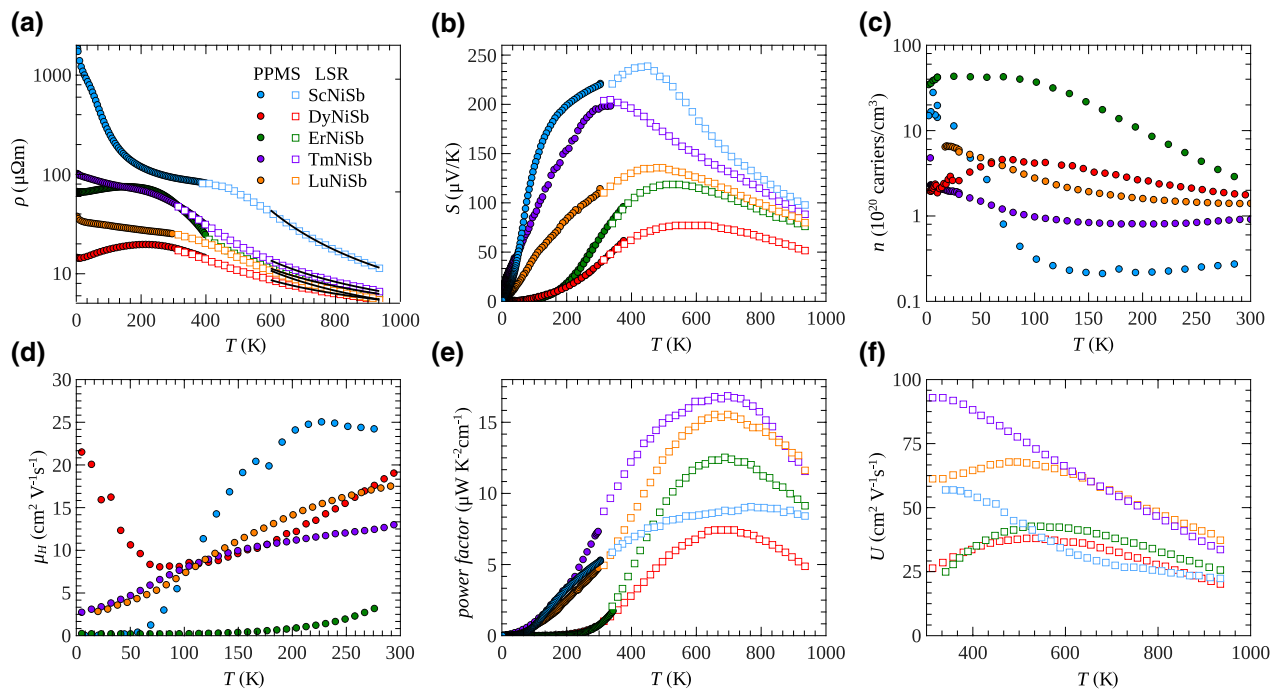


FIG. 4. Temperature dependencies of (a) electrical resistivity (note the semilogarithmic scale), (b) Seebeck coefficient, (c) Hall carrier concentration, (d) Hall mobility, (e) thermoelectric power factor (PF), and (f) weighted mobility calculated from Eq. (6) of the  $R\text{NiSb}$  specimens. Circles represent the measurements performed with the Quantum Design physical-property-measurement system (PPMS) platform, while open squares correspond to the data obtained with a Linseis LSR-3 apparatus (LSR). The solid lines in (a) denote least-squares fits of the Arrhenius law [Eq. (1)] to the experimental data above 650 K. The electrical resistivity and Seebeck-coefficient data for  $\text{ScNiSb}$  are obtained from Ref. [26].

TABLE III. Electronic transport characteristics of the  $R\text{NiSb}$  samples.  $\sigma_0$  and  $E_g$  are the parameters obtained from Eq. (1);  $E_g^*$  is the energy gap derived from Eq. (2).

$R\text{NiSb}$	$\sigma_0 (\mu\Omega^{-1} \text{ m}^{-1})$	$E_g (\text{meV})$	$E_g^* (\text{meV})$
ScNiSb	0.94(2)	383(2)	214(11)
DyNiSb	0.41(4)	130(2)	89(4)
ErNiSb	0.46(1)	170(2)	125(6)
TmNiSb	0.53(1)	205(1)	145(7)
LuNiSb	0.61(1)	193(1)	121(6)

and the so-derived parameter values are given in Table III. Remarkably, all the band gaps are found to be rather narrow. The previously published *ab initio* values of  $E_g$  for ScNiSb and LuNiSb are 0.24 and 0.20 eV, respectively [34,35]. The preliminary band structures for DyNiSb, ErNiSb, and TmNiSb result in respective band gaps of 0.31, 0.28, and 0.25 eV [49]. The experimental  $E_g$  for ScNiSb is larger than that predicted by *ab initio* calculations. Underestimation of the band gap is a common problem in density-functional-theory methods [50]. Here it should be noted that the value estimated for ScNiSb is smaller (383 meV vs 470 meV) than that derived in Ref. [26] with the formula  $1/\rho = \sigma_r + \sigma_0 \exp(-E_g/2k_B T)$ , in which an extra parameter,  $\sigma_r$ , was considered to describe residual conductivity due to the presence of disorder-related in-gap states. The previously applied model was able to cover a wider temperature range, but its accuracy of determining  $E_g$  was considerably lower [26]. In the case of other  $R\text{NiSb}$  materials, the experimental band gaps are slightly smaller than the theoretical ones. Speculatively, this phenomenon might result from the presence of crystallographic defects, which are known to reduce  $E_g$  of HH compounds [46,47,51]. Nevertheless, in none of the cases is the discrepancy between the theoretical value and the experimental value of  $E_g$  large enough to formulate a strong thesis on disorder.

It is worth noting that the electrical properties of the  $R\text{NiSb}$  samples densified by SPS are fairly similar to those of samples synthesized by single-step arc melting [31]. For both series of samples, ScNiSb has the largest electrical resistivity below 300 K, the  $\rho(T)$  variations of DyNiSb and ErNiSb show wide maxima near 200 K, and the resistivity of TmNiSb and LuNiSb varies with temperature in a quasilinear manner in the range from 100 to 300 K. Above 650 K, all the samples, regardless of the preparation method, show a behavior typical of intrinsic semiconductors. Obviously, some differences between the two series are found as regards the absolute values of the resistivity, and they can naturally be attributed to different levels of crystallographic disorder and the influence of synthesis-dependent microstructure. In addition, differently prepared samples may contain diverse secondary phases, or at least their amounts may be dissimilar in the SPS-treated specimens and the arc-melted specimens.

Figure 4(b) displays the temperature dependencies of the thermoelectric power of the  $R\text{NiSb}$  compounds. In each case, the Seebeck coefficient is positive and reaches large values, up to  $240 \mu\text{V K}^{-1}$  for ScNiSb at 450 K. According to the Goldsmid-Sharp relation ( $e$  stands for the elementary charge) [52],

$$S_{\max} = E_g^*/2eT_{\max}, \quad (2)$$

the maxima in  $S(T)$  with the coordinates  $(T_{\max}, S_{\max})$  define the Seebeck band gap  $E_g^*$ . The so-obtained values of  $E_g^*$  are notably smaller than the values of  $E_g$  found from the resistivity analysis (see Table III). As in the series of arc-melted samples [31], ScNiSb exhibits the largest thermopower among the SPS-treated  $R\text{NiSb}$  phases. Some quantitative differences between the two series can be related to dissimilar disorder effects as well as distinct synthesis-dependent microstructure of the samples. An extended comparison of the literature data available for the  $R\text{NiSb}$  compounds can be found in Ref. [31]. Theoretical predictions demonstrate that structural disorder in HH compounds, especially Ni interstitial atoms in ZrNiSn, can effectively reduce the band gap [21]. Indeed, in most reports of disordered polycrystalline materials, the experimental  $E_g$  is smaller than the band gap obtained from *ab initio* calculations; see, for example, Refs. [17,19,53]. Recently, Fu *et al.* [20] showed that high-quality ZrNiSn single crystals virtually free of interstitial atoms and subsequent in-gap electronic states exhibit a considerably larger band gap than the polycrystalline counterparts. We suggest that single-crystal growth can be an interesting way to better understanding the structural disorder in  $R\text{NiSb}$  thermoelectrics.

The temperature variations of the carrier concentration ( $n$ ) in the  $R\text{NiSb}$  samples derived from the Hall-effect measurements are shown in Fig. 4(c). At room temperature, in each compound,  $n$  amounts to about  $10^{20}$  carriers per cubic centimeter, which is an order of magnitude smaller than the values reported for the best-known optimized *p*-type HH thermoelectrics [10,13,23]. This important finding is crucial for prospective applications of the  $R\text{NiSb}$  compounds as alternative TE materials. In the Drude model, which is relevant for materials with a moderate to high concentration of noninteracting carriers, the resistivity should be inversely dependent on  $n$ :

$$\rho^{-1} = \sigma = ne\mu. \quad (3)$$

The Seebeck coefficient in the degenerate regime varies with the carrier concentration according to the following formula:

$$S = \frac{8\pi^2 k_B^2}{3eh^2} m_{\text{eff}} T \left(\frac{\pi}{3n}\right)^{2/3}, \quad (4)$$

where  $m_{\text{eff}}$  denotes the effective mass of the charge carrier. Equations (3) and (4) support the observation for

*R*NiSb ternaries of an inverse correlation of the resistivity and thermopower with  $n$ . Bearing in mind the rather-complex nature of the polycrystalline samples, each with a different rare-earth element, the qualitative agreement with the expectation should be considered satisfactory. The nonuniversal temperature dependencies of the Hall carrier concentration below 300 K are similar to the behavior reported for other HH phases [54,55].

For all the samples studied but ScNiSb, the Hall mobility ( $\mu_H$ ) continuously increases with increasing temperature above 75 K [see Fig. 4(d)]. Such behavior suggests that in these materials either ionized-impurity scattering [56] or grain-boundary scattering [57] might be the most-important charge-carrier-scattering mechanism. The finding of similar mobility curvature in an undoped ZrNiSn single crystal [58] (free from grain-boundary scattering) indicates that the influence of ionized impurities is most likely to dominate the carrier mobility in *R*NiSb compounds above 75 K. For ScNiSb,  $\mu_H$  saturates above about 200 K near a value of  $25 \text{ cm}^2 \text{ V}^{-1} \text{ s}^{-1}$ , which is similar that reported for the best HH thermoelectrics [13,30].

The experimental resistivity and thermopower data are used to calculate the temperature dependencies of the power factor ( $PF = S^2/\rho$ ) displayed in Fig. 4(e). The largest power factor of about  $17 \mu\text{W K}^{-2} \text{ cm}^{-1}$  near 700 K is found for TmNiSb, which opens a large space for optimization (e.g., by doping or improving the microstructure). This value is larger than that obtained for the arc-melted sample of the same material ( $11 \mu\text{W K}^{-2} \text{ cm}^{-1}$  at 750 K [31]) but is still within the expected range of alterations for disordered materials. In contrast, the power factor of  $9 \mu\text{W K}^{-2} \text{ cm}^{-1}$  of the SPS-treated ScNiSb sample is smaller than the power factor of  $14 \mu\text{W K}^{-2} \text{ cm}^{-1}$  of the arc-melted specimen (both at 750 K) [31]. Regardless of these findings, it should be noted that all these power factors are significantly reduced with respect to those of state-of-the-art HH thermoelectrics, which exhibit power factors as large as  $50\text{--}60 \mu\text{W K}^{-2} \text{ cm}^{-1}$  after optimization through proper charge doping [10,11,13].

Another way to compare the quality of thermoelectric materials is the weighted mobility ( $U$ ) defined by Slack [59] as

$$U = \mu_0 \left( \frac{m_{\text{eff}}}{m_e} \right)^{3/2}, \quad (5)$$

where  $\mu_0$  stands for the upper limit of mobility for the material in the intrinsic regime and  $m_e$  is the mass of a free electron. The maximum power factor achievable by tuning the carrier concentration is proportional to  $U$ , and  $U$  is related to the thermoelectric quality factor ( $B$ ) as

$$B = \left( \frac{8k_B}{3e} \right)^2 \frac{8e\pi^2(2m_e k_B T)^{3/2}}{3h^3} \frac{U}{\kappa_L} T,$$

where  $\kappa_L$  represents the lattice thermal conductivity [59]. Since electrons and holes in each material are characterized by different effective masses and mobilities,  $U$  can also be used to compare *n*-type and *p*-type transport in the same compound in order to guide the proper doping direction.

Qualitatively, in the *R*NiSb materials, dissimilar  $E_g$  values that are obtained from the Goldsmid-Sharp equation and the Arrhenius fit hint at significant differences between the weighted mobility of *n*-type and *p*-type carriers [53]. The observation of rather-low values of  $T_{\max}$  compared with values for other *p*-type HH compounds [10,13,23] indicates that the thermopower of the materials studied is influenced by minority (*n*-type) carriers with plausible superior  $U$ .

Commonly,  $U$  is quantitatively determined with use of the  $m_{\text{eff}}$  and  $\mu_0$  values calculated from the thermopower and Hall-effect data. However, especially when the Hall-effect data are not available,  $U$  of the majority carriers can be estimated by use of a formula approximating the weighted mobility in the Drude-Sommerfeld free-electron model within an accuracy of 3% for Seebeck coefficients when  $|S| > 20 \mu\text{V K}^{-1}$  [61]:

$$U = \frac{3h^3}{8\pi e(2m_e k_B T)^{3/2}} \times \frac{1}{\rho} \times \left( \frac{\exp\left(\frac{|S|}{k_B/e} - 2\right)}{1 + \exp\left[-5\left(\frac{|S|}{k_B/e} - 1\right)\right]} + \frac{\frac{3}{\pi^2} \frac{|S|}{k_B/e}}{1 + \exp\left[5\left(\frac{|S|}{k_B/e} - 1\right)\right]} \right). \quad (6)$$

After reducing the constants, one can rewrite the formula in simpler form:

$$U = 3310 \left[ \frac{\text{cm}^2}{\text{Vs}} \right] \left( \frac{1}{\rho [\mu\Omega \text{ m}]} \right) \left( \frac{T [\text{K}]}{300} \right)^{-3/2} \left( \frac{\exp\left(\frac{|S|}{k_B/e} - 2\right)}{1 + \exp\left[-5\left(\frac{|S|}{k_B/e} - 1\right)\right]} + \frac{\frac{3}{\pi^2} \frac{|S|}{k_B/e}}{1 + \exp\left[5\left(\frac{|S|}{k_B/e} - 1\right)\right]} \right), \quad (7)$$

where  $\rho$  corresponds to the electrical resistivity measured in micro-ohm meters,  $T$  denotes the temperature in kelvins,  $S$  stands for the thermopower, and  $k_B/e = 86.3 \mu\text{V K}^{-1}$ .

The so-derived temperature dependencies of  $U$  of  $p$ -type carries in the  $R\text{NiSb}$  compounds are presented in Fig. 4(f). The highest  $U$  is found for  $\text{TmNiSb}$  and  $\text{LuNiSb}$ , which is consistent with the highest power factor observed for those phases. These values are somewhat lower than the weighted mobility of the best TE materials, such as  $\text{Bi}_2\text{Te}_3$  ( $U = 250 \text{ cm}^2 \text{ V}^{-1} \text{ s}^{-1}$  near room temperature [62]) or  $\text{Na}_y\text{Co}_3\text{Sb}_{12}$  skutterudites ( $U = 340 \text{ cm}^2 \text{ V}^{-1} \text{ s}^{-1}$  at 300 K [63]), yet are comparable with those of other well-known thermoelectrics, such as  $p$ -type  $\text{PbTe}$  ( $U = 130 \text{ cm}^2 \text{ V}^{-1} \text{ s}^{-1}$  at 300 K and  $60 \text{ cm}^2 \text{ V}^{-1} \text{ s}^{-1}$  at 600 K [64]) or HH phases (e.g.,  $\text{FeV}_{1-x}\text{Nb}_x\text{Sb}$  with  $U = 60 \text{ cm}^2 \text{ V}^{-1} \text{ s}^{-1}$  at 300 K [13]).

According to the parabolic band model (PBM) [65], the Seebeck coefficient depends on the chemical potential ( $\eta$ ) in the following manner:

$$S = \frac{k_B}{e} \left( \frac{2F_1(\eta)}{F_0} - \eta \right), \quad (8)$$

where  $F_j(\eta)$  is the Fermi integral of order  $j$ ,

$$F_j(\eta) = \int_0^\infty \frac{\zeta^j (d\zeta)}{1 + \exp(\zeta - \eta)}. \quad (9)$$

Furthermore, the same PBM predicts a simple correlation between the Hall concentration of majority  $p$ -type carriers and their effective mass:

$$n = 4\pi \left( \frac{2m_{\text{eff}}k_B T}{h^2} \right)^{3/2} F_{1/2}(\eta). \quad (10)$$

The values of  $m_{\text{eff}}$  at 300 K determined from Eq. (10) are collected in Table IV. Clearly, all the  $R\text{NiSb}$  compounds investigated, except  $\text{TmNiSb}$ , are light-carrier  $p$ -type conductors with  $m_{\text{eff}}$  close to the mass of a free electron. For  $\text{ErNiSb}$ ,  $m_{\text{eff}} = 1.17m_e$  is almost equal to the experimental value of  $1.2m_e$  reported before [66]. In the case of  $\text{ScNiSb}$  and  $\text{LuNiSb}$ , *ab initio* calculations performed for the ideal  $\text{MgAgAs}$ -type model with a modified-Beck-Johnson-potential local-density approximation yield the band masses of  $p$ -type carriers  $m_b$  of  $0.36m_e$  and  $0.23m_e$ , respectively [34,35]. From the formula [67]

$$m_{\text{eff}} = N_v^{2/3} m_b, \quad (11)$$

where  $N_v$  is the degeneracy of the valence bands [in  $R\text{NiSb}$ ,  $N_v = 6$  at the  $\Gamma$  point [34]], one finds  $m_{\text{eff}} = 1.19m_e$  and  $0.76m_e$  for  $\text{ScNiSb}$  and  $\text{LuNiSb}$ , respectively. These values are somewhat smaller than the experimental findings ( $1.52m_e$  for  $\text{ScNiSb}$  and  $1.40m_e$  for  $\text{LuNiSb}$ ). The discrepancy can be attributed to structural disorder (e.g., split

positions of Ni [26] or vacancies at the Ni site [29] previously found for  $\text{ScNiSb}$ ) that was not taken into account during *ab initio* calculations [34].

To cross-check the validity of Eq. (6), which was proposed very recently [61], the intrinsic mobility  $\mu_0$  of  $p$ -type charge carriers at 300 K was determined with the PBM formula [68]

$$\mu_H = \mu_0 \frac{F_{-1/2}}{2F_0}, \quad (12)$$

and then the effective mass  $m_{\text{eff}-H}$  was extracted from the equation

$$U = \mu_0 \left( \frac{m_{\text{eff}-H}}{m_e} \right)^{3/2}. \quad (13)$$

Remarkably, the so-obtained effective masses are similar to those calculated within the Fermi-integral formalism (see Table IV), which proves the reliability of our method of estimating the weighted mobility without knowing the Hall data.

As a next step in the characterization of the electronic properties of the  $R\text{NiSb}$  materials, the carrier scattering time  $\tau$  at 300 K is calculated from the formula

$$\mu_0 = e\tau/m_{\text{eff}}. \quad (14)$$

The so-obtained values of  $\tau$  are given in Table IV. In the case of  $\text{ScNiSb}$  and  $\text{LuNiSb}$ , these data can be compared with the results of *ab initio* calculations performed within the deformation-potential theory [69], assuming predominant scattering charge carriers on acoustic phonons. According to Refs. [34,35], in these two compounds,  $\tau = 1.21 \times 10^{-14}$  and  $5.61 \times 10^{-14}$  s, respectively. The discrepancies (see Table IV) can be attributed to structural disorder in the real samples, but they may also originate from the presence of additional scattering mechanisms, such as grain-boundary or alloy scattering. It is worth mentioning that knowledge of the actual value of  $\tau$  is crucial in advanced *ab initio* searches for alternative thermoelectrics among HH phases, which are conducted in terms of the constant-relaxation-time approximation [70–73].

### C. Heat capacity

Figure 5(a) shows the temperature dependences of the specific heat ( $C_p$ ) of the nonmagnetic compounds  $\text{ScNiSb}$  and  $\text{LuNiSb}$ . Near 300 K,  $C_p$  is close to the Dulong-Petit limit of  $3n_aR = 74.8 \text{ J mol}^{-1} \text{ K}^{-1}$ . Below 7 K,  $C_p$  varies with  $T^3$  [see the inset in Fig. 5(a)], as predicted by the Debye model. The so-obtained Sommerfeld coefficients are  $\gamma = 0.5(1)$  and  $0.8(2) \text{ mJ K}^{-2} \text{ mol}^{-1}$ , for the Sc-based and Lu-based antimonide, respectively. These small values of  $\gamma$  are consistent with low electrical conductivity

TABLE IV. Electronic transport characteristics of the  $R\text{NiSb}$  samples: effective mass from the PBM  $m_{\text{eff}}$  [Eq. (10)], intrinsic  $p$ -type mobility  $\mu_0$  [Eq. (12)], effective mass from weighted mobility cross-check  $m_{\text{eff-}U}$  [Eq. (13)], mean  $p$ -type-carrier scattering time  $\tau$  [Eq. (14)], Lorenz factor  $L$  [Eq. (18)], and PBM-derived Lorenz factor  $L^*$  [Eq. (19)].

$R\text{NiSb}$	$m_{\text{eff}} (m_e)$	$\mu_0 (\text{cm}^2 \text{ V}^{-1} \text{ s}^{-1})$	$m_{\text{eff-}U} (m_e)$	$\tau (10^{-14} \text{ s})$	$L (10^{-8} \Omega \text{ W K}^{-2})$	$L^* (10^{-8} \Omega \text{ W K}^{-2})$
ScNiSb	1.52	30.6	1.60	2.78	1.65	1.60
DyNiSb	0.56	53.5	0.63	1.80	2.23	2.32
ErNiSb	1.17	10.9	1.21	0.76	2.08	2.14
TmNiSb	2.61	17.1	3.09	2.68	1.69	1.63
LuNiSb	1.53	29.1	1.40	2.66	1.89	1.87

in both materials. As displayed in Fig. 5(a), the measured  $C_p(T)$  data can be well approximated in the entire temperature range measured by the Debye formula corrected for anharmonicity [74]:

$$C_p = \gamma T + \frac{9n_a R}{1 - \alpha T} \left( \frac{T}{\Theta_D} \right)^3 \int_0^{\Theta_D/T} \frac{x^4 \exp(x)}{[\exp(x) - 1]^2} dx, \quad (15)$$

where  $\Theta_D$  represents the Debye temperature,  $\alpha$  is the anharmonicity factor, and  $x = h\nu/k_B T$ . In the least-squares fitting of Eq. (15) to the experimental data, the values of  $\gamma$  determined at low temperatures are used. The analyses yields  $\Theta_D = 354(1)$  K and  $\alpha = 0.97(6) \times 10^{-4} \text{ K}^{-1}$  for ScNiSb and  $\Theta_D = 271(1)$  K and  $\alpha = 1.5(1) \times 10^{-4} \text{ K}^{-1}$  for LuNiSb. The values of  $\Theta_D$  obtained are similar to those reported in the literature for other HH antimonides [31,55, 75]. The anharmonicity contribution to  $C_p$  is broadly similar to that of other known intermetallics [76,77] and can be speculatively described as a disorder-related effect [78].

The specific heat  $C_p(T)$  of DyNiSb, ErNiSb, and TmNiSb is presented in Fig. 5(b). Above approximately 20 K, the measured data form a nearly universal curve that approaches  $3n_a R$  near room temperature. Below 3 K, the specific heat of DyNiSb exhibits a  $\lambda$ -shaped maximum [see the inset in Fig. 5(b)] that signals the antiferromagnetic phase transition reported in the literature [39,79]. For the other two materials  $C_p(T)$  shows some upturns with decreasing temperature, which might be tentatively associated with magnetic fluctuations in a critical region of some hypothetical magnetic ordering that possibly sets in below the lowest temperature measured. The minuscule discontinuity in  $C_p(T)$  of ErNiSb near 3 K might result from antiferromagnetic ordering in the contaminant  $\text{Er}_2\text{O}_3$ , which is characterized by the Neél temperature of 3.4 K [80].

To determine the Debye temperature of ErNiSb, DyNiSb, and TmNiSb the following equation is applied [81]:

$$\frac{\Theta_D(R\text{NiSb})}{\Theta_D(\text{LuNiSb})} = \left( \frac{M_{\text{Lu}}^{3/2} + M_{\text{Ni}}^{3/2} + M_{\text{Sb}}^{3/2}}{M_R^{3/2} + M_{\text{Ni}}^{3/2} + M_{\text{Sb}}^{3/2}} \right)^{1/3}, \quad (16)$$

where  $M$  is molar mass of the corresponding atoms. The so-estimated Debye temperatures are 277 K, 275, and 274 K for Dy-bearing, Er-bearing, and Tm-bearing phases, respectively. To cross-check the applicability of this approach to the materials examined,  $\Theta_D$  is calculated from Eq. (16) also for ScNiSb. The result is  $\Theta_D = 339$  K, which is in reasonably good agreement with the experimental value of 354 K.

On the basis of the anticipated similarity of the phonon spectra of ErNiSb, DyNiSb, and TmNiSb to the phonon spectrum of LuNiSb, corroborated by nearly the same values of  $\Theta_D$ , the magnetic contribution  $\Delta C_{\text{magn}}$  to the specific heat of the compounds bearing partially filled 4f electron shells, is estimated by subtraction of the specific heat measured for LuNiSb from the experimental  $C_p(T)$  data of the  $R\text{NiSb}$  phases with  $R = \text{Dy, Er, and Tm}$ . In this approach, we assume that the anharmonicity effect and the Sommerfeld contribution in all these compounds are of similar magnitude. Then the so-derived  $\Delta C_{\text{magn}}(T)$  variations are analyzed in terms of the Schottky formula, which accounts for the crystalline electric field (CEF) effect:

$$\Delta C_{\text{magn}} = \frac{\sum_i g_i e^{-\Delta_i/T} \sum_i g_i \Delta_i^2 e^{-\Delta_i/T} - (\sum_i g_i \Delta_i e^{-\Delta_i/T})^2}{T^2 (\sum_i g_i \Delta_i e^{-\Delta_i/T})^2}, \quad (17)$$

where  $g_i$  corresponds to the degeneracy of the  $i$ th CEF level and  $\Delta_i$  is the energy separation of this level from the ground state.

Figure 5(c) shows the result of least-squares fitting of Eq. (17) to  $\Delta C_{\text{magn}}(T)$  for ErNiSb. In this compound, the ground multiplet  ${}^4I_{15/2}$  of the  $\text{Er}^{3+}$  ion splits in a cubic electric field potential into two doublets and three quartets [82]. As can be inferred from the Fig. 5(c), one can obtain a reasonably good description of the experimental data above 10 K for a doublet for the ground state and excited CEF levels being a doublet located at  $\Delta_1 = 6.7(3)$  K and three quartets with energies  $\Delta_2 = 86(2)$  K,  $\Delta_3 = 115(2)$  K, and  $\Delta_4 = 160(4)$  K. This CEF scheme differs from the model derived by means of an inelastic-neutron-scattering experiment [60], which indicated a quartet as the ground state, and the subsequent levels as a quartet, a doublet, a quartet and a doublet separated from the ground-state quartet by energies 91, 108, 160, and

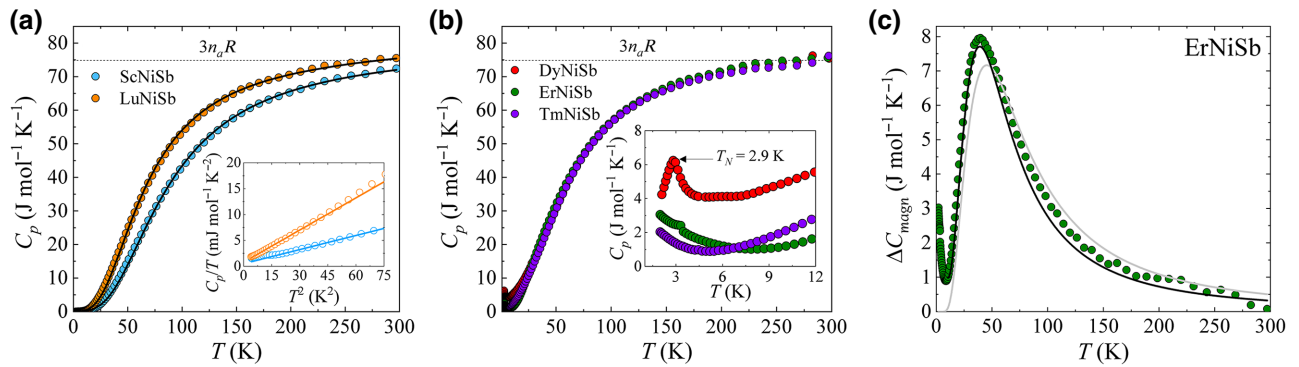


FIG. 5. (a) Temperature dependencies of the specific heat of ScNiSb and LuNiSb. Solid lines represent the least-squares fits of the Debye model. The dotted line corresponds to the Dulong-Petit limit. The inset displays the low-temperature  $C_p(T)$  data plotted as a function of temperature squared. The solid colored lines emphasize linear behavior. (b) Temperature variations of specific heat for DyNiSb, ErNiSb, and TmNiSb. The inset shows the data in the low-temperature region. (c) Analysis of the CEF effect for ErNiSb. The solid line denotes our fit of Eq. (17) and the gray line represents previous neutron-scattering results from Ref. [60].

220 K, respectively [see the gray line in Fig. 5(c)]. Speculatively, the discrepancy between the two sets of CEF levels can be attributed to dissimilar synthesis-dependent atomic disorder in different ErNiSb samples examined.

Similar analyses of the Shottky contribution to the specific heat are made for DyNiSb and TmNiSb; the results are presented in Fig. S1 in Supplemental Material [83]. In the case of the  $Dy^{3+}$  ion located in a cubic CEF potential, the multiplet  $^6H_{15/2}$  splits into two doublets and three quartets [82], as for  $Er^{3+}$ . The best description of the  $\Delta C_{\text{magn}}(T)$  data in terms of Eq. (17) yield a doublet-doublet-quartet-pseudo-octet (two degenerate quartets) CEF scheme, and the energies  $\Delta_1 = 23(1)$  K,  $\Delta_2 = 65(1)$  K, and  $\Delta_{3,4} = 153(3)$  K. In turn, for the ground-state multiplet  $^3H_6$  of the non-Kramers ion  $Tm^{3+}$ , one expects in a cubic crystal field the presence of two singlets, a doublet, and three triplets [82]. The calculations performed lead to a doublet as the ground state, and excited CEF levels being a singlet, a singlet, and three triplets located at energies  $\Delta_1 = 3.4(3)$  K,  $\Delta_2 = 31(3)$  K,  $\Delta_3 = 69(1)$  K,  $\Delta_4 = 128(3)$  K, and  $\Delta_5 = 170(5)$  K.

## D. Thermal transport

The temperature dependencies of the thermal conductivity in the  $RNiSb$  samples are shown in Fig. 6(a). The overall shape of  $\kappa(T)$  with a maximum near 50 K and a broad minimum located in the region from 400 to 600 K, observed for all these compounds, is characteristic of crystalline narrow-gap semiconductors. At 300 K, the magnitude of  $\kappa$  in DyNiSb, ErNiSb, TmNiSb, and LuNiSb, measured in the experiment with the NETZSCH LFA 457 device, is relatively small ( $3.5\text{--}5.9$  W m<sup>-1</sup> K<sup>-1</sup>). These values are smaller than those reported for archetypal HH thermoelectrics before optimization (6.3 W m<sup>-1</sup> K<sup>-1</sup> for HfNiSn, 8 W m<sup>-1</sup> K<sup>-1</sup> for ZrNiSn, and 9 W m<sup>-1</sup> K<sup>-1</sup> for TiNiSn [84], 13 W m<sup>-1</sup> K<sup>-1</sup> for VFeSb [24], and

9 W m<sup>-1</sup> K<sup>-1</sup> for ZrCoBi [10]), yet are comparable to those of other rare-earth-bearing HH compounds (e.g., 5 W m<sup>-1</sup> K<sup>-1</sup> for HoPdSb [24], 3.5 W m<sup>-1</sup> K<sup>-1</sup> for ErPdSb [55], and 2.8 W m<sup>-1</sup> K<sup>-1</sup> for YPtSb [85]). Thus, all four antimonides investigated can be considered as good candidates for alternative TE materials, especially if their electronic transport behavior is optimized. In the case of ScNiSb, the thermal conductivity at 300 K is larger than yet still comparable to that of the other pristine HH compounds listed above. The SPS-treated ScNiSb and TmNiSb samples exhibit somewhat different  $\kappa(T)$  in comparison with the solely-arc-melted specimens [31]. This finding provides another indication of the influence of the synthesis method and impurities obtained on the transport properties of the  $RNiSb$  compounds.

Figure 6(b) shows an exemplary analysis of the thermal conductivity in TmNiSb (the results obtained for the other  $RNiSb$  phases can be found in Fig. S2 in Supplemental Material [83]). In the steady-state experiment, the measured data are significantly affected in the region from 200 to 300 K by radiative losses. To account for this effect, the low-temperature experimental data are corrected by subtraction of  $\kappa_{\text{rad}} \propto T^3$  [see the dashed curve in Fig. 6(b)] in such a way as to reach at 300 K a value of  $\kappa_{\text{corr}} = \kappa - \kappa_{\text{rad}}$  equal to the thermal conductivity observed at this temperature in the experiment with the NETZSCH LFA 457 device.

In the next step, the polar electronic contribution to the thermal conductivity [ $\kappa_{\text{el-polar}}$ ; see the black squares in Fig. 6(b)] is calculated from the Wiedemann-Franz law,  $\kappa_{\text{el-polar}} = LT/\rho$ , where  $L$  is the Lorenz number. From the formula [86]

$$L = 1.5 + \exp(-|S|/116), \quad (18)$$

where  $S$  is expressed in the unit of microvolts per kelvin and  $L$  is expressed in the unit of  $10^{-8} \Omega \text{W K}^{-2}$ ,  $L =$

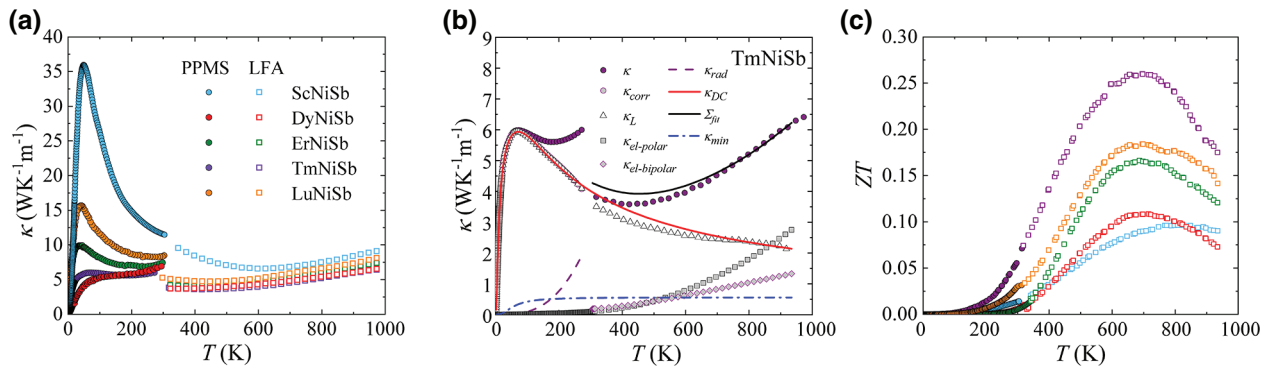


FIG. 6. (a) Temperature dependencies of the thermal conductivity of the  $R\text{NiSb}$  materials. Circles denote the data obtained with PPMS-9 (PPMS), squares correspond to the experiments performed with the NETZSCH LFA 457 device (LFA). The data for ScNiSb are taken from Ref. [26]. (b) Analysis of the thermal-conductivity data for TmNiSb; for explanation, see the main text. (c) Thermoelectric figure of merit of the  $R\text{NiSb}$  compounds as a function of temperature.

$1.69 \times 10^{-8} \Omega \text{ W K}^{-2}$  is found for TmNiSb at 300 K. Another way to determine  $L$  is provided by the PBM formalism [65]. The expression

$$L^* = \left( \frac{k_B}{e} \right)^2 \frac{3F_0(\eta)F_2(\eta) - 4F_1(\eta)^2}{F_0(\eta)} \quad (19)$$

yields for TmNiSb a value of  $1.63 \times 10^{-8} \Omega \text{ W K}^{-2}$ , which is in very good agreement with the former estimate. Also for the other  $R\text{NiSb}$  compounds, Eqs. (18) and (19) give mutually very similar values of  $L$  and  $L^*$  (see Table IV), which proves the validity of the approach applied.

By subtraction of  $\kappa_{el-polar}(T)$  from  $\kappa_{corr}(T)$ , the lattice thermal conductivity ( $\kappa_L$ ) is determined [see the red triangles in Fig. 6(b)]. Below 300 K, these data are analyzed in terms of the Debye-Callaway (DC) model [87,88]:

$$\kappa_L = \frac{k_B}{2\pi^2 v_s} \left( \frac{k_B T}{\hbar} \right)^3 \int_0^{\Theta_D/T} \frac{\tau_c x^4 e^x}{(e^x - 1)^2} dx, \quad (20)$$

where  $x = \hbar\omega/k_B T$ . The phonon relaxation time ( $\tau$ ) is calculated assuming the contributions due to umklapp ( $\tau_U$ ), point-defect-scattering ( $\tau_{pd}$ ), and grain-boundary-scattering ( $\tau_b$ ) processes:

$$\tau^{-1} = \tau_U^{-1} + \tau_{pd}^{-1} + \tau_b^{-1}, \quad (21)$$

$$\tau_U^{-1} = BT\omega^2 \exp(-C/T), \quad (22)$$

$$\tau_{pd}^{-1} = A\omega^4 = \frac{V}{4\pi v_s^3} \Gamma \omega^3, \quad (23)$$

$$\tau_b^{-1} = \frac{v_s}{r}, \quad (24)$$

where  $B$  stands for the umklapp-scattering parameter,  $C$  is the umklapp-scattering temperature coefficient,  $A$  corresponds to the point-defect-scattering constant,  $V$  denotes the average volume per atom,  $\Gamma$  is the disorder-scattering

factor, and  $r$  represents the grain size. The sound velocity ( $v_s$ ) is calculated from the Debye model:

$$v_s = \frac{k_B \Theta_D}{\hbar (6\pi^2 N)^{1/3}}, \quad (25)$$

where  $N$  is the density of atoms. The so-obtained value of  $v_s$  in TmNiSb is  $2518 \text{ m s}^{-1}$ . The results derived for the other  $R\text{NiSb}$  compounds are listed in Table V. In all these materials but ScNiSb, the sound velocity is about  $2500 \text{ m s}^{-1}$ , which is similar to  $v_s$  in the bismuthide ZrCoBi, which is considered the smallest sound velocity in the state-of-the-art HH thermoelectrics [10]. Damped  $v_s$  is desired for TE materials as it is usually associated with an inherently small magnitude of the thermal conductivity [89]. For ScNiSb,  $v_s = 3169 \text{ m s}^{-1}$  is found, which is similar to the values reported in the literature for other HH phases [30,88,90].

Fitting the DC model to the experimental data for TmNiSb yields a satisfactory description of  $\kappa_L(T)$  below 300 K [see the solid red line in Fig. 6(b) labeled as  $\kappa_{DC}$ ]. Similarly good approximations are obtained for the other  $R\text{NiSb}$  compounds investigated (see Fig. S2 in Supplemental Material [83]), apart from DyNiSb, for which the multiphase character of the specimen hinders Callaway fitting. The parameters obtained are listed in Table V. The umklapp-scattering coefficients obtained are similar to those obtained for other HH compounds [88,90]. In turn, the point-defect-scattering parameter  $\Gamma$  is found to increase on going from ScNiSb via LuNiSb to ErNiSb to TmNiSb, reaching values comparable with those obtained for HH alloys in which point-defect disorder was intentionally introduced by doping [88,90]. This finding is likely related to the sizable amount of crystallographic defects in  $R\text{NiSb}$  compounds. By comparing ScNiSb and TmNiSb between the SPS-densified and the arc-melted [26] series, one can notice qualitative agreement between nonstoichiometry detected by

TABLE V. Parameters obtained from the thermal-conductivity analysis for the  $R\text{NiSb}$  materials: umklapp-scattering coefficient  $B$ , umklapp temperature parameter  $C$ , point-defect-scattering constant  $A$ , point-defect-scattering factor  $\Gamma$ , grain size  $r$  [Eqs. (20)–(24)], sound velocity  $v_s$  [Eq. (25)], and mobility ratio  $b$  [Eq. (26)].

$R\text{NiSb}$	$B (10^{-18} \text{ K}^{-1} \text{ s})$	$C (\text{K})$	$A (10^{-42} \text{ s}^3)$	$\Gamma$	$r (10^{-6} \text{ m})$	$v_s (\text{m s}^{-1})$	$b$
ScNiSb	3.92(2)	96(1)	0.19(1)	0.0033(1)	1.0(1)	3169(9)	7.9(2)
ErNiSb	2.95(9)	51(7)	6.95(21)	0.057(1)	4.6(3)	2530(9)	19.9(2)
TmNiSb	1.81(5)	154(7)	17.2(47)	0.139(9)	3.4(1)	2518(9)	31.5(4)
LuNiSb	4.98(6)	55(6)	1.82(2)	0.014(1)	1.8(1)	2484(9)	19.7(3)

EDS and the strength of point defects of phonons revealed by Callaway fitting. In the case of ScNiSb, the sample compressed by SPS is more ordered and its EDS-derived composition is  $\text{Sc}_{1.00(1)}\text{Ni}_{0.97(1)}\text{Sb}_{0.99(1)}$  [26], while for the arc-melted specimen the composition is  $\text{Sc}_{1.00(1)}\text{Ni}_{0.88(1)}\text{Sb}_{0.99(1)}$  [31]. According to expectations, point-defect scattering of phonons is smaller for the SPS-sintered sample ( $\Gamma = 0.0033$ ) than for the arc-melted ScNiSb ( $\Gamma = 0.026$ ) [31]. In turn, for TmNiSb the SPS-densified specimen exhibits a bigger deviation from the ideal stoichiometry,  $\text{Tm}_{1.00(3)}\text{Ni}_{0.78(5)}\text{Sb}_{0.89(3)}$ , than its arc-melted counterpart,  $\text{Tm}_{1.00(2)}\text{Ni}_{0.97(2)}\text{Sb}_{0.89(2)}$  [12]. In this case also the point-defect scattering follows the tendencies in EDS-derived chemical formulas. For more-disordered SPS-densified TmNiSb, the scattering is large,  $\Gamma = 0.139$ , while for the arc-melted TmNiSb, the effect is less pronounced,  $\Gamma = 0.106$  [31]. The crystallographic disorder in  $R\text{NiSb}$  materials appears to be strongly sample dependent. Here it is necessary to mention that the EDS-derived chemical composition can have sizable errors. Further study focused on the details of the crystal structure in the studied compound family (e.g., by synchrotron-radiation XRD) appears necessary. The magnitude of the average size of grains is determined from the DC analysis for the  $R\text{NiSb}$  samples is typical of that for non-nanostructurized materials.

To summarize the aforementioned findings, the largest thermal conductivity in the  $R\text{NiSb}$  series, found for ScNiSb, can be rationalized by the observation of a rather-high sound velocity in this antimonide its relatively low density, and its high Debye temperature. In turn, the smallest  $\kappa$  value, established for TmNiSb, is associated with high density of the compound, its small  $\Theta_D$ , and small  $v_s$  as well as its very strong point-defect scattering. Here it is necessary to mention that the thermal conductivity of  $R\text{NiSb}$  materials can also be affected by the impurities. However, this influence is assumed to be rather minor due to lack of percolation paths and the small volume of the impurities for all the  $R\text{NiSb}$  materials apart from DyNiSb.

As an extension of the analysis of the low-temperature  $\kappa(T)$  data, also the heat transport in  $R\text{NiSb}$  at high temperatures is examined quantitatively. For this purpose, we assume that in the region of intrinsic conductivity a contribution due to bipolar electronic excitations ( $\kappa_{\text{el-bipolar}}$ ) must be taken into account. The temperature dependencies

of the bipolar term are calculated with the formula [32, 91–93]

$$\kappa_{\text{el-bipolar}} = \frac{b}{(b+1)^2} \left( \frac{E_g}{k_B T} + 4 \right)^2 \left( \frac{k_B}{T} \right) \sigma T, \quad (26)$$

where  $b$  is the mobility ratio of charge carriers,  $\sigma$  is the measured electrical conductivity, and  $E_g$  is the intrinsic energy gap (see Table III). Least-squares fitting of Eq. (26) is performed to the total thermal conductivity subtracted with lattice contribution obtained from the Callaway model and the polar electronic part:  $\kappa_{\text{total}} - \kappa_{\text{DC}} - \kappa_{\text{el-polar}}$ . The results obtained for TmNiSb are displayed in Fig. 6(b) (see the open diamonds), and those derived for the other samples studied are shown in Fig. S2 in Supplemental Material [83]. The parameter  $b$  was found to span from 8 in ScNiSb to 32 in TmNiSb (see Table V). Such large values of the mobility ratio between  $n$ -type and  $p$ -type carriers (here predominance of electrons is most likely) appears fully consistent with the observed differences between the energy gaps  $E_g$  and  $E_g^*$  calculated from the Arrhenius and Goldsmid-Sharp formulas, respectively (see above).

As can be inferred from Fig. 6(b) (see the open black triangles), the lattice contribution to the thermal conductivity of TmNiSb at elevated temperatures, calculated as  $\kappa_L = \kappa_{\text{total}} - \kappa_{\text{el-polar}} - \kappa_{\text{el-bipolar}}$ , agrees with the DC prediction  $\kappa_{\text{DC}}(T)$  [represented in Fig. 6(b) by the solid red line] that is constructed only on the basis of the low-temperature data. Similarly good agreement is obtained for the other  $R\text{NiSb}$  compounds considered (see Fig. S2 in Supplemental Material [83]), which proves the relevance of our approach. Another visualization of the overall validity of the analyses comes from the comparison of the experimental  $\kappa$  data collected at high temperatures with the function  $\Sigma_{\text{fit}} = \kappa_{\text{DC}} + \kappa_{\text{el-polar}} + \kappa_{\text{el-bipolar}}$ , traced in Fig. 6(b) by a solid black curve (see also similar curves in Fig. S2 in Supplemental Material [83]). Bearing in mind several simplifications made in the bipolar-thermal-conductivity model, such as the single parabolic character of valence and conduction bands, fully intrinsic behavior, and acoustic phonon interaction as the only carrier-scattering mechanism [32], the agreement between the calculated data and those measured experimentally appears very good, especially at elevated temperatures, where the  $R\text{NiSb}$  materials can be considered intrinsic semiconductors.

The minimal lattice thermal conductivity ( $\kappa_{\min}$ ) can be calculated with the Cahill formula [94]:

$$\kappa_{\min} = \left( \frac{3n}{4\pi} \right)^{1/3} \frac{k_B^2 T^2}{\hbar \Theta_D} \int_0^{\Theta_D/T} \frac{x^3 e^x}{(e^x - 1)^2} dx. \quad (27)$$

The results obtained for TmNiSb [see the dashed-dotted line in Fig. 6(b)] and the other *R*NiSb phases (see Fig. S2 in Supplemental Material [83]) indicate that for each compound  $\kappa_{\min}(T)$  is much smaller in the entire temperature range considered than the experimental  $\kappa(T)$ . This finding opens a perspective of significantly reducing the thermal conductivity in these materials by proper electronic and/or phonon engineering, such as alloying or nanostructurization.

From the experimental data collected for the *R*NiSb compounds, one can calculate the thermoelectric figure of merit ( $ZT = S^2 T \rho^{-1} \kappa^{-1}$ ); the results are shown in Fig. 6(c). The maximum value of  $ZT$  of 0.25 at 700 K is obtained for TmNiSb. On the basis of the findings for this material, its best TE performance is mostly governed by intrinsic structural disorder, which brings about strong point-defect scattering of phonons and an enhanced effective mass, which implies high weighted mobility and hence a large magnitude of the power factor.

#### IV. CONCLUSIONS

We synthesize polycrystalline specimens of DyNiSb, ErNiSb, TmNiSb, and LuNiSb by arc melting with subsequent spark plasma sintering, and comprehensively characterize their structural, electronic transport and thermodynamic behaviors. The heat-capacity data for nonmagnetic ScNiSb and LuNiSb are successfully described in terms of the anharmonicity-corrected Debye model, while the data for DyNiSb, ErNiSb, and TmNiSb are reasonably modeled by our taking into account the crystal electric field effect. All the *R*NiSb samples examined are found to be intrinsic *p*-type semiconductors with an energy gap not exceeding 0.4 eV. For DyNiSb, ErNiSb, TmNiSb, and LuNiSb, the experimental band gaps are gently reduced with respect to the theoretically predicted results, which might result from the presence of crystallographic defects producing in-gap states. The Hall mobility increases with increasing temperature from 2 to 300 K, which indicates grain-boundary and/or ionized-impurity interactions being the main carrier-scattering mechanisms. The power factor determined for these materials is large, attaining for TmNiSb a value of  $17 \mu\text{W K}^{-2} \text{cm}^{-1}$  at 700 K. The same sample shows the highest value of  $ZT$  of 0.25 at 700 K. The effective mass determined from the PBM ranges from as low as  $0.56m_e$  for DyNiSb to  $2.61m_e$  for TmNiSb, which may reflect different levels and types of defects in distinct *R*NiSb samples. For the Tm-based sample, the weighted mobility calculated from thermopower and resistivity data

is found to be large as  $93 \text{ cm}^2 \text{ V}^{-1} \text{ s}^{-1}$  at room temperature. By comparing these results with those derived from the PBM formalism, we successfully verify an approximate expression for  $U$ . Using the parabolic band model, we also estimate the electronic relaxation time  $\tau$  in the *R*NiSb phases to be  $0.8 \times 10^{-14}$ – $2.8 \times 10^{-14}$  s. The measured rather-low thermal conductivity in these materials ( $\kappa = 3$ – $6 \text{ W m}^{-1} \text{ K}^{-1}$ ) is explained as a result of a low sound velocity of about  $2500 \text{ m s}^{-1}$  and strong point-defect scattering due to significant disorder in the crystal structure. Remarkably, the bipolar-thermal-conductivity analysis indicates rapid minority-carrier activation at temperatures as low as 300–600 K. This abnormal feature implies a large mobility ratio between minority (*n*-type) and majority (*p*-type) charge carriers, which opens a prospective for achieving superior thermoelectric performance in the *R*NiSb compounds on their proper electron doping. Reduction of the experimental band gap with respect to theoretical values, anharmonicity detected in heat-capacity analysis, and enhanced point-defect scattering of phonons suggest jointly that further studies of *R*NiSb materials focused on determining precisely the structural disorder might be very fruitful.

#### ACKNOWLEDGMENT

This work was supported by the National Science Centre (Poland) under MAESTRO Grant No. 2015/18/A/ST3/00057.

- [1] M. Hirschberger, S. Kushwaha, Z. Wang, Q. Gibson, S. Liang, C. A. Belvin, B. A. Bernevig, R. J. Cava, and N. P. Ong, The chiral anomaly and thermopower of Weyl fermions in the half-Heusler GdPtBi, *Nat. Mater.* **15**, 1161 (2016).
- [2] J. A. Logan, S. Patel, S. D. Harrington, C. Polley, B. D. Schultz, T. Balasubramanian, A. Janotti, A. Mikkelsen, and C. J. Palmstrøm, Observation of a topologically non-trivial surface state in half-Heusler PtLuSb (001) thin films, *Nat. Commun.* **7**, 1 (2016).
- [3] Z. Nourbakhsh, Three dimensional topological insulators of LuPdBixSb<sub>1-x</sub> alloys, *J. Alloys Compd.* **549**, 51 (2013).
- [4] Y. Nakajima, R. Hu, K. Kirshenbaum, A. Hughes, P. Syers, X. Wang, K. Wang, R. Wang, S. R. Saha, and D. Pratt *et al.*, Topological RPdBi half-Heusler semimetals: A new family of noncentrosymmetric magnetic superconductors, *Sci. Adv.* **1**, e1500242 (2015).
- [5] O. Pavloviuk, D. Kaczorowski, X. Fabreges, A. Gukasov, and P. Wiśniewski, Antiferromagnetism and superconductivity in the half-Heusler semimetal HoPdBi, *Sci. Rep.* **6**, 18797 (2016).
- [6] M. Hundley, J. Thompson, P. Canfield, and Z. Fisk, Electronic transport properties of the semimetallic heavy fermion YbBiPt, *Phys. Rev. B* **56**, 8098 (1997).

- [7] D. Kaczorowski, A. Leithe-Jasper, P. Rogl, H. Flandorfer, T. Cichorek, R. Pietri, and B. Andraka, Magnetic, thermodynamic, and electrical transport properties of ternary equiatomic ytterbium compounds  $\text{YbTM}$  ( $T$  = transition metal,  $M$  = Sn and Bi), *Phys. Rev. B* **60**, 422 (1999).
- [8] F. Casper and C. Felser, Giant magnetoresistance in semiconducting  $\text{DyNiBi}$ , *Solid State Commun.* **148**, 175 (2008).
- [9] J. Pierre and I. Karla, Giant magnetoresistance in  $RE\text{NiSb}$  semiconductors ( $RE$  = Tb, Dy, Ho), *J. Magn. Magn. Mater.* **217**, 74 (2000).
- [10] H. Zhu, R. He, J. Mao, Q. Zhu, C. Li, J. Sun, W. Ren, Y. Wang, Z. Liu, and Z. Tang *et al.*, Discovery of  $\text{ZrCoBi}$  based half Heuslers with high thermoelectric conversion efficiency, *Nat. Commun.* **9**, 1 (2018).
- [11] S.-W. Kim, Y. Kimura, and Y. Mishima, High temperature thermoelectric properties of  $\text{TiNiSn}$ -based half-Heusler compounds, *Intermetallics* **15**, 349 (2007).
- [12] K. Synoradzki, K. Ciesielski, L. Kępiński, and D. Kaczorowski, Power factor enhancement in a composite based on the half-Heusler antimonide  $\text{TmNiSb}$ , *J. Appl. Phys.* **123**, 235101 (2018).
- [13] C. Fu, T. Zhu, Y. Liu, H. Xie, and X. Zhao, Band engineering of high performance  $p$ -type  $\text{FeNbSb}$  based half-Heusler thermoelectric materials for figure of merit  $zT > 1$ , *Energy Environ. Sci.* **8**, 216 (2015).
- [14] G. Rogl, A. Grytsiv, M. Gürth, A. Tavassoli, C. Ebner, A. Wünschek, S. Puchegger, V. Soprunya, W. Schranz, and E. Bauer *et al.*, Mechanical properties of half-Heusler alloys, *Acta Mater.* **107**, 178 (2016).
- [15] E. Rausch, B. Balke, S. Ouardi, and C. Felser, Long-term stability of  $(\text{Ti/Zr/Hf})\text{CoSb}_{1-x}\text{Sn}_x$  thermoelectric  $p$ -type half-Heusler compounds upon thermal cycling, *Energy Tech.* **3**, 1217 (2015).
- [16] C. Yu, T.-J. Zhu, R.-Z. Shi, Y. Zhang, X.-B. Zhao, and J. He, High-performance half-Heusler thermoelectric materials  $\text{Hf}_{1-x}\text{Zr}_x\text{NiSn}_{1-y}\text{Sb}_y$  prepared by levitation melting and spark plasma sintering, *Acta Mater.* **57**, 2757 (2009).
- [17] H.-H. Xie, J.-L. Mi, L.-P. Hu, N. Lock, M. Christensen, C.-G. Fu, B. B. Iversen, X.-B. Zhao, and T.-J. Zhu, Interrelation between atomic switching disorder and thermoelectric properties of  $\text{ZrNiSn}$  half-Heusler compounds, *CrystEngComm* **14**, 4467 (2012).
- [18] H. Xie, H. Wang, C. Fu, Y. Liu, G. J. Snyder, X. Zhao, and T. Zhu, The intrinsic disorder related alloy scattering in  $\text{ZrNiSn}$  half-Heusler thermoelectric materials, *Sci. Rep.* **4**, 6888 (2014).
- [19] K. S. Kim, Y.-M. Kim, H. Mun, J. Kim, J. Park, A. Y. Borisevich, K. H. Lee, and S. W. Kim, Direct observation of inherent atomic-scale defect disorders responsible for high-performance  $\text{Ti}_{1-x}\text{Hf}_x\text{NiSn}_{1-y}\text{Sb}_y$  half-Heusler thermoelectric alloys, *Adv. Mater.* **29**, 1702091 (2017).
- [20] C. Fu, M. Yao, X. Chen, L. Z. Maulana, X. Li, J. Yang, K. Imasato, F. Zhu, G. Li, and G. Auffermann *et al.*, Revealing the intrinsic electronic structure of 3D half-Heusler thermoelectric materials by angle-resolved photoemission spectroscopy, *Adv. Sci.* **7**, 1902409 (2020).
- [21] P. Larson, S. Mahanti, and M. Kanatzidis, Structural stability of Ni-containing half-Heusler compounds, *Phys. Rev. B* **62**, 12754 (2000).
- [22] C. Fu, S. Bai, Y. Liu, Y. Tang, L. Chen, X. Zhao, and T. Zhu, Realizing high figure of merit in heavy-band  $p$ -type half-Heusler thermoelectric materials, *Nat. Commun.* **6**, 1 (2015).
- [23] H. Zhu, J. Mao, Y. Li, J. Sun, Y. Wang, Q. Zhu, G. Li, Q. Song, J. Zhou, and Y. Fu *et al.*, Discovery of  $\text{TaFeSb}$ -based half-Heuslers with high thermoelectric performance, *Nat. Commun.* **10**, 1 (2019).
- [24] D. Young, P. Khalifah, R. Cava, and A. Ramirez, Thermoelectric properties of pure and doped  $\text{FeMSb}$  ( $M$  = V, Nb), *J. Appl. Phys.* **87**, 317 (2000).
- [25] S. Sportouch, P. Larson, M. Bastea, P. Brazis, J. Ireland, C. Kannewurf, S. Mahanti, C. Uher, and M. G. Kanatzidis, Observed properties and electronic structure of  $RE\text{NiSb}$  compounds ( $R$  = Ho, Er, Tm, Yb and Y), potential thermoelectric materials, *Mater. Res. Soc. Symp. Proc.* **545**, 421 (1999).
- [26] K. Synoradzki, K. Ciesielski, I. Veremchuk, H. Borrman, P. Skokowski, D. Szymański, Y. Grin, and D. Kaczorowski, Thermal and electronic transport properties of the half-Heusler phase  $\text{ScNiSb}$ , *Materials* **12**, 1723 (2019).
- [27] K. Ciesielski, D. Gnida, H. Borrman, R. Ramlau, Y. Prots, D. Szymański, Y. Grin, and D. Kaczorowski, Structural, thermodynamic and magnetotransport properties of half-Heusler compound  $\text{HoPtSb}$ , *J. Alloys Compd.* **829**, 154467 (2020).
- [28] V. Romaka, L. Romaka, A. Horyn, P. Rogl, Y. Stadnyk, N. Melnychenko, M. Orlovskyy, and V. Krayovskyy, Peculiarities of thermoelectric half-Heusler phase formation in  $\text{Gd-Ni-Sb}$  and  $\text{Lu-Ni-Sb}$  ternary systems, *J. Solid State Chem.* **239**, 145 (2016).
- [29] T. Harmening, H. Eckert, and R. Pöttgen, Defects in half-Heusler type antimonides  $\text{ScTSb}$  ( $T$  = Ni, Pd, Pt), *Solid State Sci.* **11**, 900 (2009).
- [30] H. Xie, H. Wang, Y. Pei, C. Fu, X. Liu, G. J. Snyder, X. Zhao, and T. Zhu, Beneficial contribution of alloy disorder to electron and phonon transport in half-Heusler thermoelectric materials, *Adv. Funct. Mater.* **23**, 5123 (2013).
- [31] K. Ciesielski, K. Synoradzki, I. Wolańska, P. Stachowiak, L. Kępiński, A. Jeżowski, T. Toliński, and D. Kaczorowski, High-temperature power factor of half-Heusler phases  $RE\text{NiSb}$  ( $RE$  = Sc, Dy, Ho, Er, Tm, Lu), *J. Alloys Compd.* **816**, 152596 (2020).
- [32] C. Glassbrenner and G. A. Slack, Thermal conductivity of silicon and germanium from 3 K to the melting point, *Phys. Rev.* **134**, A1058 (1964).
- [33] I. Wolańska, K. Synoradzki, K. Ciesielski, K. Załęski, P. Skokowski, and D. Kaczorowski, Enhanced thermoelectric power factor of half-Heusler solid solution  $\text{Sc}_{1-x}\text{Tm}_x\text{NiSb}$  prepared by high-pressure high-temperature sintering method, *Mater. Chem. Phys.* **227**, 29 (2019).
- [34] M. J. Winiarski, K. Bilińska, K. Ciesielski, and D. Kaczorowski, Thermoelectric performance of  $p$ -type half-Heusler alloys  $\text{ScMSb}$  ( $M$  = Ni, Pd, Pt) by *ab initio* calculations, *J. Alloys Compd.* **762**, 901 (2018).
- [35] M. J. Winiarski and K. Bilińska, High thermoelectric power factors of  $p$ -type half-Heusler alloys  $\text{YNiSb}$ ,  $\text{LuNiSb}$ ,  $\text{YPdSb}$ , and  $\text{LuPdSb}$ , *Intermetallics* **108**, 55 (2019).

- [36] K. Synoradzki, K. Ciesielski, L. Kępiński, and D. Kaczorowski, Thermoelectric properties of  $(\text{DyNiSn})_{1-x}(\text{DyNiSb})_x$  composite, *Physica B* **536**, 659 (2018).
- [37] K. Ciesielski, K. Synoradzki, I. Wolańska, P. Stuglik, and D. Kaczorowski, High-temperature thermoelectric properties of half-Heusler phases  $\text{Er}_{1-x}\text{Ho}_x\text{NiSb}$ , *Mater. Today: Proc.* **8**, 562 (2019).
- [38] K. Synoradzki, K. Ciesielski, L. Kępiński, and D. Kaczorowski, Effect of secondary LuNiSn phase on thermoelectric properties of half-Heusler alloy LuNiSb, *Mater. Today: Proc.* **8**, 567 (2019).
- [39] K. Synoradzki, K. Ciesielski, and D. Kaczorowski, Magnetocaloric effect in antiferromagnetic half-Heusler alloy DyNiSb, *Acta Phys. Pol. A* **133**, 691 (2018).
- [40] O. Pavloviuk, D. Kaczorowski, and P. Wiśniewski, Shubnikov-de Haas oscillations, weak antilocalization effect and large linear magnetoresistance in the putative topological superconductor LuPdBi, *Sci. Rep.* **5**, 9158 (2015).
- [41] O. Pavloviuk, D. Kaczorowski, and P. Wiśniewski, Superconductivity and Shubnikov-de Haas oscillations in the noncentrosymmetric half-Heusler compound YPtBi, *Phys. Rev. B* **94**, 035130 (2016).
- [42] R. Weast, M. Astle, and W. Beyer, in *CRC Handbook of Chemistry and Physics: A Ready-Reference Book of Chemical and Physical Data* (CRC Press, Boca Raton, 1984), 65th ed.
- [43] L. Akselrud and Y. Grin, Wincsd: Software package for crystallographic calculations (version 4), *J. Appl. Crystallogr.* **47**, 803 (2014).
- [44] I. Karla, J. Pierre, and R. Skolozdra, Physical properties and giant magnetoresistance in RNiSb compounds, *J. Alloys Compd.* **265**, 42 (1998).
- [45] S. Stoyko, O. Zhak, S. Oryshchyn, V. Babizhetskyy, and K. Hiebl, Crystal structure and physical properties of the ternary antimonides  $R_3\text{Ni}_6\text{Sb}_5$ ,  $R = \text{Y}, \text{Gd}, \text{Tb}$ , *J. Alloys Compd.* **602**, 1 (2014).
- [46] S. Öğüt and K. M. Rabe, Band gap and stability in the ternary intermetallic compounds  $\text{NiSn}M$  ( $M = \text{Ti}, \text{Zr}, \text{Hf}$ ): A first-principles study, *Phys. Rev. B* **51**, 10443 (1995).
- [47] K. Kirievsky, D. Fuks, and Y. Gelbstein, Composition conserving defects and their influence on the electronic properties of thermoelectric TiNiSn, *Phys. Chem. Chem. Phys.* **22**, 8035 (2020).
- [48] I. Antonyshyn, F. R. Wagner, M. Bobnar, O. Sichevych, U. Burkhardt, M. Schmidt, M. König, K. Poeppelmeier, A. P. Mackenzie, E. Svanidze, and Y. Grin, Microscale device—an alternative route for studying the intrinsic properties of solid-state materials: The case of semiconducting TaGeIr, *Angew. Chem. Int. Ed.* **59**, 11136 (2020).
- [49] A. Jain, S. P. Ong, G. Hautier, W. Chen, W. D. Richards, S. Dacek, S. Cholia, D. Gunter, D. Skinner, and G. Ceder et al., Commentary: The materials project: A materials genome approach to accelerating materials innovation, *APL Mater.* **1**, 011002 (2013).
- [50] J. P. Perdew and A. Zunger, Self-interaction correction to density-functional approximations for many-electron systems, *Phys. Rev. B* **23**, 5048 (1981).
- [51] G. Y. Yonggang, X. Zhang, and A. Zunger, Natural off-stoichiometry causes carrier doping in half-Heusler filled tetrahedral structures, *Phys Rev. B* **95**, 085201 (2017).
- [52] H. Goldsmid and J. Sharp, Estimation of the thermal band gap of a semiconductor from Seebeck measurements, *J. Electron. Mater.* **28**, 869 (1999).
- [53] J. Schmitt, Z. M. Gibbs, G. J. Snyder, and C. Felser, Resolving the true band gap of ZrNiSn half-Heusler thermoelectric materials, *Mater. Horiz.* **2**, 68 (2015).
- [54] K. Gofryk, D. Kaczorowski, T. Plackowski, A. Leithe-Jasper, and Y. Grin, Magnetic and transport properties of the rare-earth-based Heusler phases  $RPdZ$  and  $RPd_2Z$  ( $Z = \text{Sb}, \text{Bi}$ ), *Phys. Rev. B* **72**, 094409 (2005).
- [55] K. Gofryk, D. Kaczorowski, T. Plackowski, J. Mucha, A. Leithe-Jasper, W. Schnelle, and Y. Grin, Magnetic, transport, and thermal properties of the half-Heusler compounds ErPdSb and YPdSb, *Phys. Rev. B* **75**, 224426 (2007).
- [56] J. Mao, J. Shuai, S. Song, Y. Wu, R. Dally, J. Zhou, Z. Liu, J. Sun, Q. Zhang, and C. Dela Cruz et al., Manipulation of ionized impurity scattering for achieving high thermoelectric performance in *n*-type  $\text{Mg}_3\text{Sb}_2$ -based materials, *Proc. Natl. Acad. Sci. USA* **114**, 10548 (2017).
- [57] J. J. Kuo, S. D. Kang, K. Imasato, H. Tamaki, S. Ohno, T. Kanno, and G. J. Snyder, Grain boundary dominated charge transport in  $\text{Mg}_3\text{Sb}_2$ -based compounds, *Energy Environ. Sci.* **11**, 429 (2018).
- [58] Q. Ren, C. Fu, Q. Qiu, S. Dai, Z. Liu, T. Masuda, S. Asai, M. Hagihala, S. Lee, S. Torri, T. Kamiyama, L. He, X. Tong, C. Felser, D. J. Singh, T. Zhu, J. Yang, and J. Ma, Establishing the carrier scattering phase diagram for ZrNiSn-based half-Heusler thermoelectric materials, *Nat. Commun.* **11**, 3142 (2020).
- [59] G. A. Slack, in *CRC handbook of thermoelectrics* (CRC Press, Boca Raton, Florida, 1995), p. 407.
- [60] I. Karla, J. Pierre, A. Murani, and M. Neumann, Crystalline electric field in RNiSb compounds investigated by inelastic neutron scattering, *Physica B* **271**, 294 (1999).
- [61] G. J. Snyder, A. H. Snyder, M. Wood, R. Gurunathan, B. H. Snyder, and C. Niu, Weighted mobility, *Adv. Mater.* **32**, 2001537 (2020).
- [62] W. Liu, K. C. Lukas, K. McEnaney, S. Lee, Q. Zhang, C. P. Opeil, G. Chen, and Z. Ren, Studies on the  $\text{Bi}_2\text{Te}_3-\text{Bi}_2\text{Se}_3-\text{Bi}_2\text{S}_3$  system for mid-temperature thermoelectric energy conversion, *Energy Environ. Sci.* **6**, 552 (2013).
- [63] Y. Pei, J. Yang, L. Chen, W. Zhang, J. Salvador, and J. Yang, Improving thermoelectric performance of caged compounds through light-element filling, *Appl. Phys. Lett.* **95**, 042101 (2009).
- [64] Y. Pei, A. D. LaLonde, H. Wang, and G. J. Snyder, Low effective mass leading to high thermoelectric performance, *Energy Environ. Sci.* **5**, 7963 (2012).
- [65] H. J. Goldsmid, *Introduction to Thermoelectricity* (Springer, Berlin, 2010), Vol. 121.
- [66] K. Kawano, K. Kurosaki, H. Muta, and S. Yamanaka, Substitution effect on the thermoelectric properties of *p*-type half-Heusler compounds:  $\text{ErNi}_{1-x}\text{Pd}_x\text{Sb}$ , *J. Appl. Phys.* **104**, 013714 (2008).
- [67] Y. Pei, H. Wang, and G. J. Snyder, Band engineering of thermoelectric materials, *Adv. Mater.* **24**, 6125 (2012).

- [68] P. M. Böttger, G. S. Pomrehn, G. J. Snyder, and T. G. Finstad, Doping of *p*-type ZnSb: Single parabolic band model and impurity band conduction, *Phys. Status Solidi A* **208**, 2753 (2011).
- [69] J. Bardeen and W. Shockley, Deformation potentials and mobilities in non-polar crystals, *Phys. Rev.* **80**, 72 (1950).
- [70] M. Zeeshan, J. van den Brink, and H. C. Kandpal, Hole-doped cobalt-based Heusler phases as prospective high-performance high-temperature thermoelectrics, *Phys. Rev. Mater.* **1**, 074401 (2017).
- [71] M. K. Yadav and B. Sanyal, First principles study of thermoelectric properties of Li-based half-Heusler alloys, *J. Alloys Compd.* **622**, 388 (2015).
- [72] J. Kangsabanik, A. Alam, and Vikram, Bismuth based half-Heusler alloys with giant thermoelectric figures of merit, *J. Mater. Chem. A* **5**, 6131 (2017).
- [73] T. Fang, S. Zheng, H. Chen, H. Cheng, L. Wang, and P. Zhang, Electronic structure and thermoelectric properties of *p*-type half-Heusler compound NbFeSb: A first-principles study, *RSC Adv.* **6**, 10507 (2016).
- [74] C. Martin, Simple treatment of anharmonic effects on the specific heat, *J. Phys.: Condens. Matter* **3**, 5967 (1991).
- [75] I. Skovsen, L. Bjerg, M. Christensen, E. Nishibori, B. Balke, C. Felser, and B. B. Iversen, Multi-temperature synchrotron PXRD and physical properties study of half-Heusler TiCoSb, *Dalton Trans.* **39**, 10154 (2010).
- [76] P. Svoboda, J. Vejpravova, N.-T. Kim-Ngan, and F. Kaysel, Specific heat study of selected *R*Ni<sub>5</sub>, *J. Magn. Magn. Mater.* **272**, 595 (2004).
- [77] K. Procházková, S. Danis, and P. Svoboda, Specific heat study of PrNi<sub>4</sub>Si, *Acta Phys. Pol. A* **113**, 299 (2008).
- [78] P. Zalden, K. S. Siegert, S. Rols, H. E. Fischer, F. Schlich, T. Hu, and M. Wuttig, Specific heat of (GeTe)<sub>x</sub>(Sb<sub>2</sub>Te<sub>3</sub>)<sub>1-x</sub> phase-change materials: The impact of disorder and anharmonicity, *Chem. Mater.* **26**, 2307 (2014).
- [79] I. Karla, J. Pierre, and B. Ouladdiaf, Magnetic structures of *R*NiSb compounds (*R* = rare earths) investigated by neutron diffraction, *Physica B* **253**, 215 (1998).
- [80] R. M. Moon, W. C. Koehler, H. R. Child, and L. J. Raubenheimer, Magnetic structures of Er<sub>2</sub>O<sub>3</sub> and Yb<sub>2</sub>O<sub>3</sub>, *Phys. Rev.* **176**, 722 (1968).
- [81] M. Bouvier, P. Lethuillier, and D. Schmitt, Specific heat in some gadolinium compounds. I. Experimental, *Phys. Rev. B* **43**, 13137 (1991).
- [82] K. Lea, M. Leask, and W. Wolf, The raising of angular momentum degeneracy of *f*-electron terms by cubic crystal fields, *J. Phys. Chem. Solids* **23**, 1381 (1962).
- [83] See Supplemental Material at <http://link.aps.org/supplemental/10.1103/PhysRevApplied.14.054046>, for Figs. S1 and S2.
- [84] H. Hohl, A. P. Ramirez, W. Kaefer, K. Fess, C. Thurner, C. Kloc, and E. Bucher, A new class of materials with promising thermoelectric properties: *M*NiSn(*M* = Ti, Zr, Hf), *MRS Proc.* **478**, 109 (1997).
- [85] S. Ouardi, G. H. Fecher, C. Felser, J. Hamrle, K. Postava, and J. Pištora, Transport and optical properties of the gapless Heusler compound PtYSb, *Appl. Phys. Lett.* **99**, 211904 (2011).
- [86] H.-S. Kim, Z. M. Gibbs, Y. Tang, H. Wang, and G. J. Snyder, Characterization of Lorenz number with Seebeck coefficient measurement, *APL Mater.* **3**, 041506 (2015).
- [87] J. Callaway, Model for lattice thermal conductivity at low temperatures, *Phys. Rev.* **113**, 1046 (1959).
- [88] A. Petersen, S. Bhattacharya, T. Tritt, and S. Poon, Critical analysis of lattice thermal conductivity of half-Heusler alloys using variations of Callaway model, *J. Appl. Phys.* **117**, 035706 (2015).
- [89] E. S. Toberer, A. Zevalkink, and G. J. Snyder, Phonon engineering through crystal chemistry, *J. Mater. Chem* **21**, 15843 (2011).
- [90] T. Zhu, C. Fu, H. Xie, Y. Liu, B. Feng, J. Xie, and X. Zhao, Lattice thermal conductivity and spectral phonon scattering in FeVSb-based half-Heusler compounds, *Europhys. Lett.* **104**, 46003 (2013).
- [91] B. I. Davydov and I. M. Shmushkevitch, *Uspekhi Fiz. Nauk USSR* **24**, 21 (1940).
- [92] P. Price, CXXXV. Ambipolar thermodiffusion of electrons and holes in semiconductors, *London Edinb. Dublin Philos. Mag. J. Sci.* **46**, 1252 (1955).
- [93] J. R. Drabble and H. J. Goldsmid, *Thermal Conduction in Semiconductors* (Pergamon, Oxford, 1961), Vol. 4.
- [94] D. G. Cahill, S. K. Watson, and R. O. Pohl, Lower limit to the thermal conductivity of disordered crystals, *Phys. Rev. B* **46**, 6131 (1992).